

Electronic structure of the surface states of the Zr_3SnC_2 MAX phaseTakahiro Ito ^{1,2,*}, Thierry Ouisse,^{3,†} Manaya Mita,² Kiyohisa Tanaka,⁴ Laurent Jouffret,⁵
Hanna Pazniak ³ and Serge Quessada³¹*Nagoya University Synchrotron Radiation Research Center (NUSR), Nagoya University, Nagoya 464-8603, Japan*²*Graduate School of Engineering, Nagoya University, Nagoya 464-8603, Japan*³*Université Grenoble Alpes, CNRS, Grenoble INP, LMGP, F-38000 Grenoble, France*⁴*UVSOR Facility, Institute for Molecular Science, Okazaki 444-8585, Japan*⁵*Université Clermont Auvergne, CNRS, ICCF, F-63000 Clermont-Ferrand, France*

(Received 6 September 2023; revised 28 November 2023; accepted 29 November 2023; published 13 December 2023)

We synthesized cm-sized single crystals of the nanolamellar compound Zr_3SnC_2 and performed angle-resolved photoemission spectroscopy (ARPES). A challenging problem to be solved, when studying electronic structure with ARPES, is to differentiate the surface and bulk electronic bands. We found that just after cleavage, the ARPES signal of Zr_3SnC_2 is dominated by surface states with well-defined energy dispersions. The (1×1) periodicity and the very good match of the electronic structure measured by ARPES with the DFT predictions indicate the absence of surface reconstruction. Mechanical cleavage happens at the Sn-Zr plane boundary, and the ARPES results are consistent with a top surface divided into locally unaltered regions covered with Sn atoms and regions terminated with Zr atoms. We provide a thorough analysis of these surface state bands. Longer-lived surface states are attributed to the Sn-terminated areas. DFT indicates that the surface bands of the Sn-terminated surface do not only involve Sn p orbitals, but also d orbitals of the Zr atoms lying closest to the surface. The orbital nature of the surface bands is further ascertained by ARPES.

DOI: [10.1103/PhysRevB.108.235145](https://doi.org/10.1103/PhysRevB.108.235145)**I. INTRODUCTION**

MAX phases form a wide family of nanolamellar compounds, made attractive by a unique combination of ceramic and metalliclike properties [1–3], and also by the possibility to convert them chemically into two-dimensional (2D) compounds named MXenes [4,5]. The latter show a great potential for energy storage [5], among many other interesting applications. The most common stoichiometry of MAX phases is $M_{n+1}AX_n$, with M an early transition metal, A mostly belonging to groups 13–14, and $X = C$ or N . Here, we focus on Zr_3SnC_2 . The small neutron cross section of Zr, combined with the remarkable mechanical, chemical, and physical properties of MAX phases, make Zr-based MAX carbides unique candidates for nuclear fuel cladding applications [6–8]. Zr_3SnC_2 was synthesized in powder form a few years ago [8]. Most MAX phase materials are indeed produced this way, possibly sintered and compressed [2]. The polycrystalline character of those materials makes difficult the direct observation of the remarkable anisotropies resulting from their nanolamellar structure, and most particularly the anisotropies in their electronic structure. In this work, we used macroscopic-sized single crystals.

In a series of previous works, we and co-workers measured the electronic structure of several MAX phases using single crystals and angle resolved photoemission spectroscopy

(ARPES) [9–14]. In those papers, emphasis was put on the bulk electronic properties. However, we noticed that in some compounds, surface bands could also be observed [10]. These surface states, resulting from the mechanical cleavage in ultrahigh vacuum (UHV) conditions, were slowly passivated inside the UHV chamber used for the ARPES measurements [10]. Surface states often give rise to a good ARPES intensity as compared to bulk states, since (i) the mean free path of photoelectrons with a few tens eV kinetic energies is typically less than 1 nm and the probing depth is limited to the very first atomic layers [15], and (ii) their 2D character also favors a large intensity, as opposed to bulk states with a substantial k_z dispersion. In the case of Zr_3SnC_2 , the ARPES signal emanating from the surface state bands turns out to exceed the bulk contribution very substantially and gives rise to relatively long-lived ARPES signatures. This compound therefore offers the opportunity to study the 2D surface states of a MAX phase in great detail. In this paper, we analyze the physical origin and electronic structure of any of the observed surface state bands by combining ARPES measured from macroscopic single crystals and density functional theory (DFT) computations.

Surface state measurements are essential for analyzing surface reconstruction. Key indications are often provided by scanning tunneling microscopy (STM) or low energy electron diffraction (LEED). But ARPES can also provide good evidence for surface reconstruction, e.g., by the observation of surface state band folding, and give complementary and useful information about the electronic structure (see, e.g., Refs. [16–19] for cases ranging from semiconductors to

*Corresponding author: t.ito@nusr.nagoya-u.ac.jp†Corresponding author: thierry.ouisse@grenoble-inp.fr

metals and magnetic materials). In recent years, a renewed and very strong interest was induced by the rapid expansion of the research on topological materials [20]. Inversion symmetry breaking by the surface and spin-orbit coupling may lead, in topological materials, to lock the spin or the orbital momentum with the electron momentum [21,22]. This prevents the surface electrons at the Fermi energy from suffering from backscattering. It offers a way to protect those states, and to preserve and use spin polarization [20].

In our case, and in contrast with topological insulators, the surface states coexist with bulk, metallic states. But their prominent signature in the ARPES signal permits a detailed investigation. Combining DFT and ARPES allows us to identify the orbital nature of the various surface bands. To better know the electronic structure resulting from mechanical cleavage is important in two respects: On the one hand, it gives fundamental information about the formation and structure of mechanical cracks [23]. On the other hand, it sheds light on the mechanical exfoliation of MAX phases into 2D materials, which was recently shown to be possible in spite of bonds much stronger than those existing in van der Waals solids [24]. In both cases, the initial surface electronic structure governs the subsequent surface reactivity and final surface chemistry. Remarkably enough, the specific electronic structure which we observe is entirely due to surface atoms arranged in the same order as in the bulk lattice, even for the less strongly bonded ones.

II. MATERIALS AND METHODS

Crystal growth was achieved by the flux method and slow cooling, as we previously did for growing other MAX phases (see, e.g., [25–27]). However, in the case of Zr_3SnC_2 , one has to tackle the extremely low solubility of C in a tin flux, whatever the temperature T is, and the existence of the competing Zr_2SnC phase. We first checked that, as for the solution growth of Cr_2AlC [25], or even that of V_2AlC [26], using a simple Zr-Sn-C flux only results in the production of mm-sized Zr_2SnC single crystals. In order to synthesize Zr_3SnC_2 , we therefore decided to add to the flux an element enhancing C solubility while not forming any highly stable compound with the other elements involved. A candidate of choice is chromium. With the help of the available binary phase diagrams and after some preliminary attempts with different flux compositions, we used an atomic composition Zr-Sn-Cr around 15 : 42.5 : 42.5. Carbon was provided by partial dissolution of the graphite crucible. Due to the high vapor pressure of Sn, the crucible was hermetically closed and heated by induction up to 1750 °C, as measured on top of the graphite lid by a pyrometer. The flux was then slowly cooled (typically 1 week) down to 1300 °C, and then left cooling down freely to 300 K. Crystals were extracted from the solidified flux by dissolving the latter in concentrated HCl. Large single crystals were characterized by measuring Laue x-ray diffraction patterns. Elemental composition, as measured by energy dispersive x-ray analysis (EDX), confirmed that Cr was not incorporated in the crystals. Crystal structure refinement was obtained from a smaller crystal and x-ray intensity data were measured at Mo wavelength ($\lambda = 0.71073 \text{ \AA}$) on a Bruker D8 diffractometer. The frames were integrated with

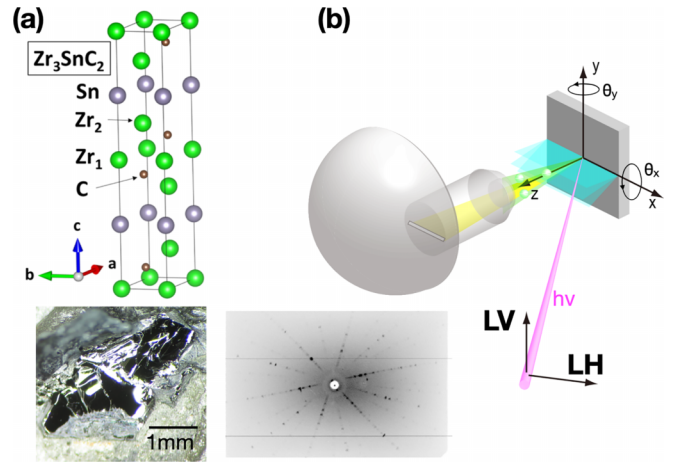


FIG. 1. (a) Crystal structure of Zr_3SnC_2 , pictured using VESTA software, along with the image of a mechanically cleaved sample and a typical Laue diffraction pattern. (b) ARPES setup used for linear polarization dependence.

the Bruker SAINT software package using a narrow-frame algorithm. Data were corrected for absorption effects using the multiscan method (SADABS), and the structure was solved and refined using the Bruker SHELXTL software package. The integration of the data using a hexagonal unit cell yielded a total of 4609 reflections (686 independent) to a maximum θ angle of 36.45° (0.60 Å resolution). The final cell constants are $a = 3.3622(5) \text{ \AA}$, $b = 3.3622(5) \text{ \AA}$, $c = 19.913(3) \text{ \AA}$, volume = 194.95(8) Å³, using the space group $P6_3/mmc$, with $Z = 2$ for the formula unit, C_2SnZr_3 . The lattice parameters obtained from the refinement were then used as input in the DFT calculations. The crystal structure is shown in Fig. 1(a) along with the picture of a single crystal after cleaving *in situ*, and a typical Laue pattern.

All calculations were carried out with the full potential LAPW+lo method implemented within the WIEN2K software. The Perdew-Burke-Ernzerhof (PBE) GGA functional was chosen [28]. Wave functions were expanded up to a RKM cut-off parameter of 7.5, where RKM is the product of the smallest muffin tin radius by the largest wavevector value. We took a k mesh of about 16 k points with a Monkhorst-Pack meshing of the irreducible Brillouin zone (BZ) for all calculations. The Fermi surfaces (FSs) were calculated using X-CRYSDEN [29]. Orbital character was obtained with the Spaghetti PRIMA.PY code available in WIEN2K. For computing the surface state bands, supercells were built with five primitive unit cells stacked along c , resulting in 59 or 61 inequivalent atoms per supercell, depending on the cut selected for defining the nature of the surface atoms. The stacked cells were separated by a vacuum gap of 2.5 nm. The five-unit cell also corresponded to 59 or 61 atomic layers along c , a number large enough for preventing any interaction between the surface states belonging to opposite surfaces in a slab, as demonstrated by the absence of noticeable splitting of the predicted surface bands into bonding and antibonding states. Around 100 iterations were required for the energy convergence to go below a threshold of 10^{-6} .

Crystals were cleaved *in situ* parallel to the basal plane for ARPES experiments performed at UVSOR BL5U and BL7U

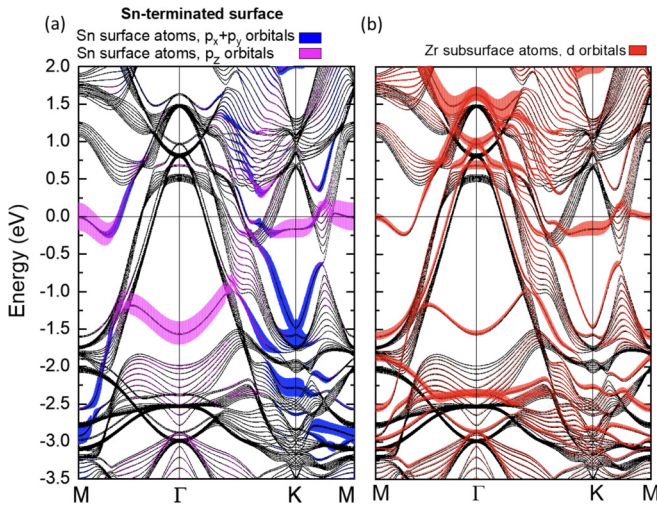


FIG. 2. Band structure of Zr_3SnC_2 , including the surface state bands induced by an Sn-terminated surface, and as computed by DFT from a five-unit supercell as described in the text. The bold color curves indicate the importance of some specific orbital contributions (curve width is proportional to the projection of the states onto the considered orbital).

lines. The UVSOR lines are equipped with a MBSscientific A-1 analyzer. The temperature was set either to 25 or 30 K. The energy resolution was set at $\Delta E \sim 38$ meV ($T = 30$ K, base pressure below 4×10^{-9} Pa) and $\Delta E \sim 20$ meV ($T = 25$ K, base pressure below 6×10^{-9} Pa) with an acceptance angle of $\pm 15^\circ$ for θ_x and $\pm 16^\circ$ for θ_y , respectively. We probed the $k_y \sim -2.0 \text{ \AA}^{-1}$ momentum region by rotating the sample holder relatively to the detector. Energy-dependent ARPES was performed using photons energies $h\nu = 21.2$ eV and 70–95 eV. The configuration used for linear polarization dependence is illustrated by Fig. 1(b). The angle between the light beam and the detector was set to 45° . The Z coordinate refers to the analyzer lens direction [see Fig. 1(b)]. Varying energy measurements (not shown in this paper) allowed us to plot ARPES versus k_z , and the observed BZ periodicity led to an inner potential value $V_0 = 17.7$ eV.

III. DENSITY FUNCTIONAL THEORY

The band structure and orbital character of the surface state bands, as computed from the built supercells, are shown in Figs. 2 and 3 in the case of an Sn-terminated and Zr-terminated surface, respectively. The supercell computation has two effects: on the one hand, it gives the surface state bands resulting from the existence of the surface. On the other hand, it gives the bulk projected bands, which are now quantized and subdivided into several bands, each of them corresponding to a quantized k_z value. Roughly speaking, the supercell calculation shows a set of bulk bands corresponding to quantized k_z values spanned over the whole Brillouin zone (in other words, if the supercell size was tending to infinity, those bands would multiply and tend to become filled areas describing the full k_z dispersion of the bands over a Brillouin zone). One can note here that the larger the k_z dispersion, the smaller becomes the expected ARPES intensity of the band under consideration (as a rule of thumb, and without

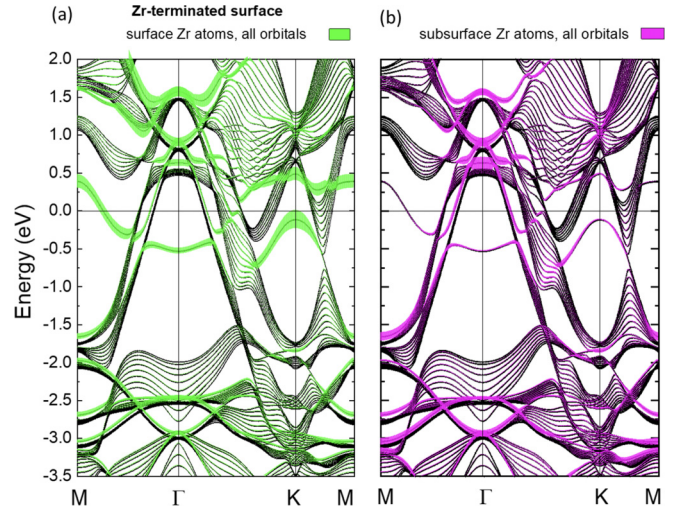


FIG. 3. Band structure of Zr_3SnC_2 , including the surface state bands induced by a Zr-terminated surface. Some orbital contributions are highlighted as described in Fig. 2.

considering orientation-dependent cross section effects, 2D dispersions preferentially result in well-defined ARPES lines, whereas k_z -dispersed bands result in lower intensity areas). In Figs. 2 and 3, we identify the surface state bands by projecting each k state onto specific atomic orbitals of the surface or subsurface atoms, and plotting the result as an additional dispersion on each band, proportional to the result found. In those two figures, we limited ourselves to show the important orbital contributions of the surface and subsurface atoms to the bands lying close to the Fermi energy (E_F).

It is worth noticing that, among the DFT bands displaying a substantial contribution of the surface and subsurface atoms, not all of them represent true surface states. The bands appearing in the gaps of the bulk bands are surface states, whereas those appearing inside the original bulk bands are surface resonances, the states of which extend throughout the whole supercell. The nature of each band was verified by using the criterion that a true surface state band does not display a noticeable contribution of atoms beyond the subsurface layer. The nature of each band (true surface state or surface resonance) is listed in Sec. IV. Besides, if Tamm states are considered as those which rather look like a linear combination of surface and subsurface atoms only, all the true surface states predicted and observed in this work are Tamm states.

We found that for the Sn-terminated surface, the surface states are not only formed of p_z and $p_x + p_y$ orbitals of the Sn surface atoms, but also involve a substantial contribution of the d orbitals of the subsurface Zr atoms (see Fig. 2). No appreciable contribution of the subsurface C atoms was noticed a few eV around E_F . It is worth noticing that the surface band with a noticeable Sn- p_z contribution roughly correspond to the result expected from a simple tight-binding (TB) model involving only the p_z orbitals of the hcp lattice formed by the Sn atoms at the surface (magenta color in Fig. 2), which would give a minimum in Γ , and show cosine-like E - k dispersion as one approaches the BZ boundaries. Yet this band is also formed of Zr d orbitals [red color in Fig. 2(b)]

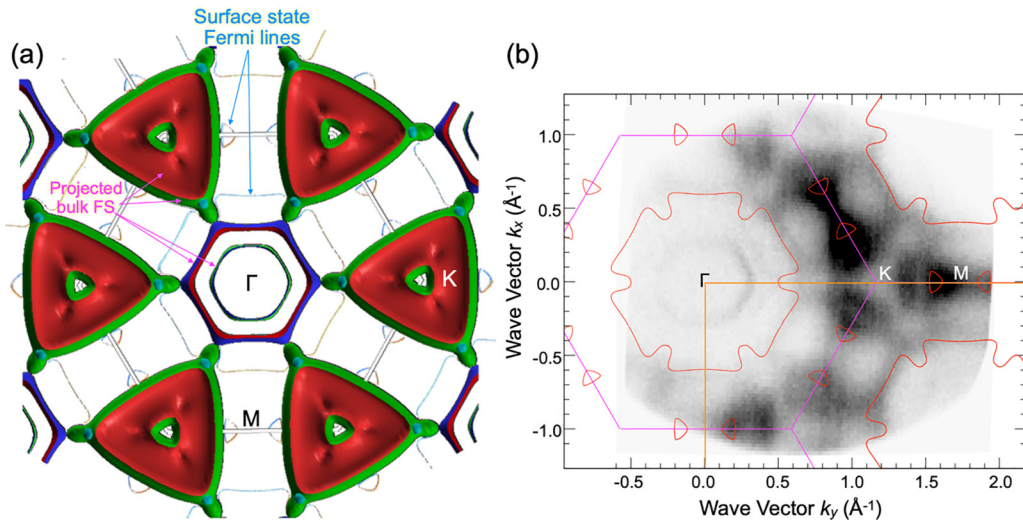


FIG. 4. (a) DFT-computed Fermi surface of Zr_3SnC_2 , including the surface state Fermi lines induced by an Sn-terminated surface. (b) ARPES Fermi surface (FS) map obtained by 71.5-eV photons, onto which are superimposed the Fermi lines due to the surface states of the Sn-terminated surface.

and is of course modified in a complex manner whenever it crosses and interacts with the bulk projected bands. Those interactions make the corresponding energies become slightly larger in M than in K , whereas the opposite should be expected from a simple TB model of the form $E = E_0 - 2\beta_0 \{\cos[a(k_x + \sqrt{3}k_y)/2] + \cos[a(k_x - \sqrt{3}k_y)/2] + \cos(ak_z)\}$. The $p_x + p_y$ -like surface bands (blue color) do not lend themselves to so simple an explanation (see their variation in Fig. 2, with a minimum located at K). The degeneracy lift of the p_z and $p_x + p_y$ dominated surface bands at their crossing (see the dispersion along ΓM in Fig. 2) gives rise to the specific saddlelike structure predicted around and centered in M . Apart from additional and necessary considerations about the orientation dependence of the photoionization cross sections, we can expect the ARPES signal intensity plots, if more sensitive to the surface bands, to roughly follow the color dispersions appearing in Figs. 2 and 3. Figure 4(a) displays the Fermi surface of the bulk compound, as well as the surface state band contribution obtained from the supercell. Roughly similar to the case of Ti_2SnC , already discussed in [14], we can make a distinction between quasi-2D hole bands centered on Γ , and 3D (filled red triangles) and quasi-2D bands centered on the K points. The surface states add to those structures two Fermi line patterns: The first one consists of small, open triangles located on the KM lines, which are due to the saddlelike structure centered in M and are the hole pockets. The second is a hexagonal flowerlike pattern centered on Γ . Both patterns could possibly give rise to an enhanced ARPES signal that cannot be attributed to bulk bands.

In the case of the Zr-terminated surface, all surface bands involve just Zr orbital contributions (Fig. 3). Close to E_F , one predicts the existence of an hcp TB-like band centered on Γ and located at energies higher than in the case of the p_z bands of the Sn-terminated surface, and an additional band centered in K with a maximum just below E_F .

IV. ARPES MEASUREMENTS AND ANALYSIS

A. Surface state band structure

Figure 5(a) superimposes the band structures of the Zr- and Sn-terminated surfaces, with a curve thickness proportional to the orbital contribution of the surface (or subsurface) atoms, as already shown in Fig. 2. Figure 5(b) shows the band structure as assessed by ARPES for the $M\Gamma KM$ k path, for a photon energy equal to 71.5 eV. Figure 5(b) represents the central result of this paper.

If one carefully compares Fig. 5(a) with Fig. 5(b), it is quite obvious that all the surface state bands predicted for an Sn- or Zr-terminated surface are also present in the experiment. Besides, we checked that varying the photon energy from 71.5 eV (Figs. 4 and 5) to 76 eV (Fig. 7) or 21.2 eV (Fig. 6) did not change the band energy positions as well as the FS shapes, a fact much in favor of the 2D character of those bands. In order to better appreciate the remarkable match between DFT and ARPES, in Fig. 5 we labeled some prominent surface state band segments as B1, B2, etc., so that they can be easily identified and compared both in Figs. 5(a) and 5(b). Let us consider first the Sn-terminated surface regions: the ARPES signal intensity reasonably matches the contribution of the surface Sn atom p_z orbitals and $p_x + p_y$ orbitals (note that those bands also include a subsurface Zr orbital contribution). The discrepancy in energy values between DFT and ARPES in each of those surface state bands does not exceed 0.2 eV, and all observed symmetries and band shapes are the same: saddlelike structure around M (B3), wide minimum around Γ (B1), the complicated band structure around K and between K and M (B2, just below E_F), and the deeper $p_x + p_y$ band centered on K (B5). Lowering all DFT surface state bands with respect to E_F by an amount around -0.15 eV would still give a better quantitative fit. Even the width of the DFT curves, proportional to the projection of the states onto the considered surface atom orbitals, seems to roughly agree with

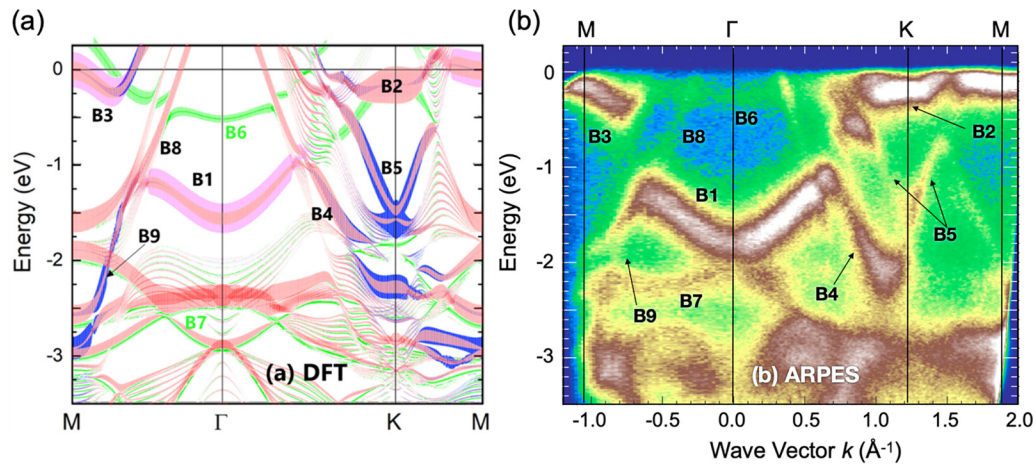


FIG. 5. (a) Band structure predicted by DFT for the same k path as shown in (b) ARPES image along the $M\Gamma KM$ wave-vector path indicated as orange lines in Fig. 4(b). Photon energy $h\nu$ was set to 71.5 eV, $T = 30$ K.

the measured ARPES intensity, whereas no photoionization cross sections effects are accounted for. We can classify each labeled band according to its main orbitals contributions, and specify if it is a surface state band (SS) or a surface resonance (SR): B1 is SS (mostly surface Sn, sp_z , and also subsurface Zr, d_z^2 and $d_{xz} + d_{yz}$), B2 and B3 are SSs (mostly surface Sn, sp_z , and also subsurface Zr, $d_{xz} + d_{yz}$), B5 is SS [surface

Sn, $s(p_x + p_y)$ and also subsurface Zr, $d_{xz} + d_{yz}$], B6 is SS (surface Zr, d band), and B7, B8, and B9 are SRs.

The predicted contribution of the Zr-terminated surface is less obvious to identify, because the corresponding signal is weaker, but it is also present in the ARPES (B6 and B7). The ARPES does display a Γ -centered, noninverted band (B6), but the minimum is around -0.25 eV, whereas the one predicted

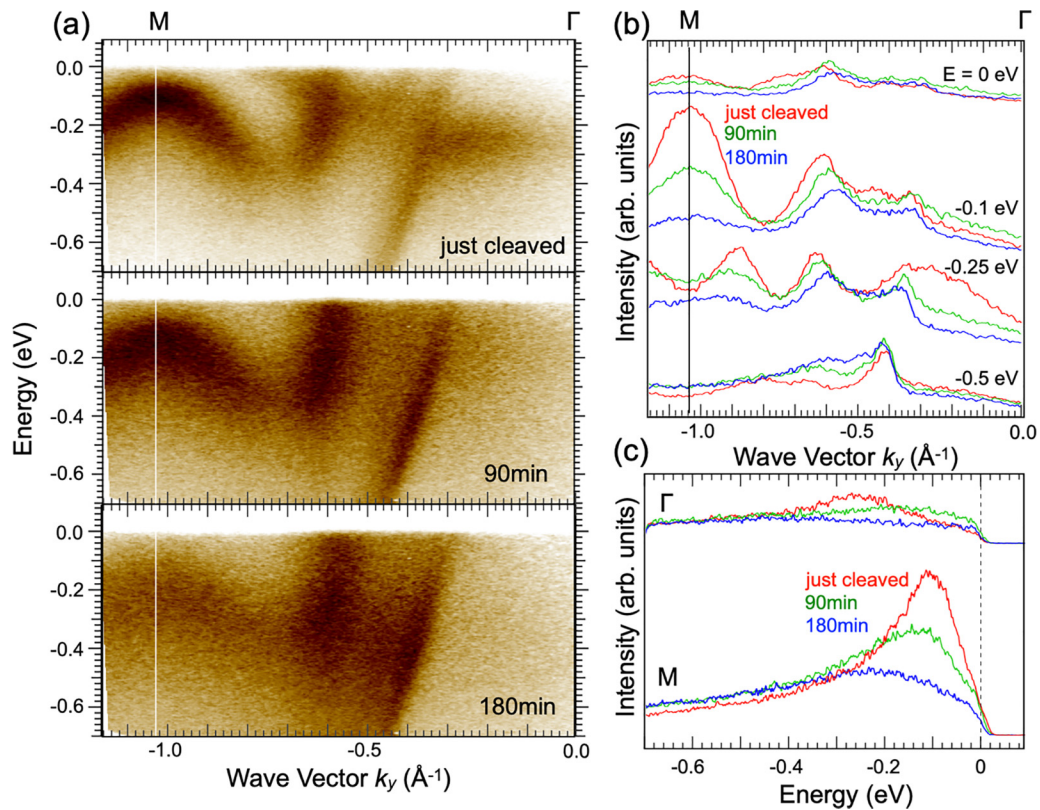


FIG. 6. Time dependence of the surface state contribution to ARPES obtained by $h\nu = 21.2$ eV. (a) Band structure along the $M\Gamma$ line at different times: just after cleaving sample (top), 90 min (middle), and 180 min (bottom) later, respectively. (b),(c) ARPES signal intensity versus k [momentum distribution curves (MDC)], measured at different times and energies (b) and ARPES signal intensity versus energy [energy distribution curves (EDC)] measured at different times in Γ and M , respectively (c).

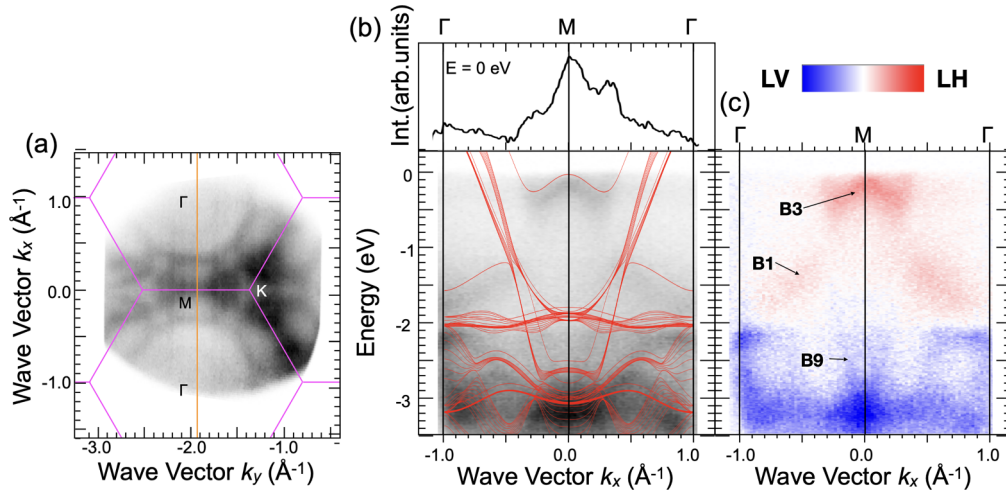


FIG. 7. FS map (a) and band structure along the ΓM line [orange line in (a)] (b) as measured by summing the ARPES signals $LV + LH$ obtained with a light beam linearly polarized along y (LV) or horizontal plane (LH), respectively [see Fig. 1(b)]. Photon energy $h\nu$ was set to 76 eV, $T = 30$ K. DFT bands of Sn-terminated surface (Fig. 2) are superimposed for direct comparison. (c) ARPES plot of the difference ($LH-LV$) in the same conditions as (b). MDC spectrum at $E = 0$ eV is indicated at upper panel of (b).

by DFT rather lies around -0.55 eV. The same can be written for band B7. Yet, their shape is the same for DFT and ARPES. Raising those DFT surface bands by around 0.3 eV would also give a quantitatively more satisfying fit of ARPES. The energy shift may be readily explained by an electron transfer from the Sn-terminated to the Zr-terminated surface, which could then raise all surface state bands by some amount in the case of the Zr-terminated surface and do the opposite for the Sn-terminated surface. Besides, the model used for DFT does not take into account a possible relaxation of the interplane distance between the top surface and the plane below, which might also induce some shift in the bands. The bulk hole bands crossing E_F and centered on Γ are well retrieved (B8), but it might also be due to the fact that the subsurface Zr atoms do participate to those dispersions (see Fig. 2), making them more apparent. Overall, it is clear that the surface-state contributions substantially prevail over the bulk ones, and are well predicted by DFT.

The strong similarity between ARPES and DFT leaves little doubt about the way the surface is structured. However, the simultaneous observation of Zr- and Sn-terminated surface contributions in the same ARPES measurement deserves some further explanation. Mechanical cleavage must happen where the bonds between two atomic basal planes are weaker, i.e., the Zr-Sn bonds. However, in order to observe surface band dispersions agreeing with the DFT predictions for Zr- or Sn-terminated surfaces, two essential conditions must also be met: On the one hand, the surface atoms must keep their bulk positions, and there must be no surface reconstruction. On the other hand, the surface must be subdivided into Sn-terminated and Zr-terminated regions with typical areas appreciably larger than the lattice parameter a . That both conditions apply to real samples was not studied for Zr_3SnC_2 , but for another MAX phase, Cr_2AlC [24]. In that previous work, we and other co-workers could, by means of scanning tunneling microscopy measurements, observe that the surface atom configuration was that of the nonreconstructed hcp 2D lattice expected for the Cr or the Al atoms. Besides, the

surface mechanically cleaved in UHV conditions was subdivided into two kinds of domains, each with a characteristic STM current signature, with typical sizes exceeding several nanometers or even larger (as shown in [24]). As in [24], what we observe here is just an additional confirmation of the way the MAX phase surface is formed under mechanical cleavage. In contrast, e.g., with the case of silicon [23], the final cleavage plane is clearly that with the smallest surface energy (although not shown here, DFT simulations starting from a surface terminated inside the Zr-C planes do not display a good agreement with ARPES). What is remarkable here is the survival of the initial, bulk structural order of the surface Sn atoms after cleavage, as indicated by the match between ARPES and DFT. In the bulk, the Sn atoms are equally well bonded to each of the two neighboring Zr atom planes, one of the two sides having to be broken during cleavage (Fig. 1). But the Zr-Sn bond strength is not negligible at all in front of the Sn-Sn bond strength. This is thus different from van der Waals solids, where the in-plane bonds are always much stronger than the out-of-plane ones, thus preserving in-plane order easily. Here, preservation of the initial order, even at a local level, is thus an interesting result. It is just as if the Sn atoms had to choose between two surfaces during the cleavage, but, at a local scale, decided to do it collectively, depending on which side was first chosen by some precursors. It is also important to notice that band B1, which can be explained by a tight-binding band mainly involving the p_z orbitals of the hcp lattice formed by the unreconstructed surface Sn atoms (see Sec. III), looks very similar to the main surface state band that we previously evidenced for V_2AlC [10]. It displays the same sinelike shape with its minimum in Γ (see Fig. 8 in [10]). This is a good indication that our result can be generalized to other (not to say many) MAX phases.

The most characteristic patterns of the predicted FS [see Fig. 4(a)] are also clearly visible in the ARPES FS map, as shown in Fig. 4(b). We note that with the configuration selected for the ARPES experiment, the photoionization cross section is larger for positive k_y values and orbital contributions

extending along z (see, e.g., the explanations given in [9]). In that region, where the ARPES intensity signal is more important, one clearly observes the triangles with p_z orbital contribution, located along the KM line and corresponding to the surface state band B2 (Fig. 4). A better fit could be obtained by slightly shifting the Fermi energy across the bands, as explained above.

B. Surface state stability

The time evolution of the surface state signal is shown in Fig. 6 for some surface state bands crossing E_F . The behaviors of the saddlelike structure attributed to the Sn-terminated surface (B3 in Fig. 5) and of the TB-like band with its minimum in Γ attributed to the Zr-terminated surface (B6 in Fig. 5) are very different. As shown in Fig. 6, pattern B3 is much more robust than pattern B6, which almost totally disappears in less than 90 min, whereas pattern B3 is still clearly measured after 180 min. Also worth noticing is the fact that the hole bulk band (or the band due to the subsurface Zr atoms of the Sn-terminated region) is always clearly visible. Those features are consistent with Zr top surface atoms oxidizing and/or being passivated faster than the Sn surface atoms. Such a mechanism might be favored by the electron transfer from the Sn- to the Zr-terminated surface which we already hypothesized for explaining the surface state energy shift between ARPES and DFT. The stability variation between patterns B3 and B6 also strengthens the assumption that they must be attributed to two different surface terminations. It is worth noticing that as surface passivation advances with time and B6 disappears, the surface band B3 progressively shifts downwards in energy, meaning that the chemical potential changes with respect to the Sn-terminated surface states after surface passivation. Such a sensitivity to a change in surface charge distribution is also consistent with explaining the energy shift between DFT and ARPES by a charge transfer between the Zr- and Sn-terminated surfaces.

C. Dependence of ARPES on the direction of linear polarization

The two configuration setups used for measuring the dependence of the ARPES signal on the polarization vector orientation are shown in Fig. 7. The two configurations give ARPES signals labeled as LH and LV , respectively. When considering the parity of orbitals relative to the mirror plane, LH favors p_x , p_z , d_{xz} , $d_{x^2-y^2}$, and d_{z^2} orbital contributions on the one hand, and LV favors p_y , d_{yz} , and d_{xy} orbitals on the other hand. Figure 7(b) shows the ARPES dispersions measured along $\Gamma M \Gamma$ as indicated with an orange line on

the Fermi surface image [Fig. 7(a)]. Figure 7(c) shows a plot of the $(LH-LV)$ signal. The more prominent surface bands are B1, B3, and B9, due to the Sn-terminated surface. As shown in Fig. 7(b), the linear polarization results confirm the DFT predictions: B1 and B3, the main orbital contribution of which is mainly Sn p_z (see Fig. 2), enhance the LH ARPES signal, whereas B9, corresponding to Sn $p_x + p_y$ (see Fig. 2), favors in turn the LV signal, until B9 crosses B1 and its main orbital nature changes, as also predicted by DFT, into p_z . Agreement between DFT and ARPES is therefore not restricted to the dispersion shapes, but also extends to the orbital nature of the surface state bands.

V. CONCLUSION

We found that Zr_3SnC_2 single crystals mechanically cleaved along their basal plane in UHV conditions are characterized by a nonreconstructed surface. The preserved hcp atomic lattices of either the Zr- or Sn-terminated surfaces give rise to the existence of surface state bands with characteristic and well-defined energy dispersions. Just after mechanical cleavage, the contribution of those surface bands to the ARPES signal largely prevails over the bulk one. Those surface state dispersions can be satisfactorily retrieved and explained by DFT. Since the lack of surface reconstruction was already foreseen from STM measurements conducted on another phase (Cr_2AlC [24]), and also because very similar surface state bands were already observed in the case of a third one (V_2AlC [10]), this result can probably be generalized to many MAX phases. This implies that the possible existence of useful surface topological properties could reasonably be studied by DFT for all MAX phases, assuming a nonreconstructed surface as that observed in this work. Such properties might then be directly tested using single crystals and spin-polarized or circularly polarized ARPES.

ACKNOWLEDGMENTS

The ARPES experiments using synchrotron light were conducted at both UVSOR BL5U and BL7U lines. The authors acknowledge the experimental assistance of BL5U and BL7U of UVSOR-III synchrotron beamline staff. This work was supported by JSPS KAKENHI Grant No. 17K05495. The ARPES experiments using synchrotron light were conducted at UVSOR-III BL5U (Proposals No. 21-664, No. 21-853, and No. 22IMS6652) and BL7U (Proposals No. 21-685, No. 21-870, and No. 22IMS6664).

- [1] H. Nowotny, Strukturchemie einiger Verbindungen der Übergangsmetalle mit den elementen C, Si, Ge, Sn, *Prog. Solid State Chem.* **5**, 27 (1971).
- [2] M. W. Barsoum, *MAX Phases* (Wiley, Weinheim, 2013).
- [3] M. Sokol, V. Natu, S. Kota and M. W. Barsoum, On the chemical diversity of the MAX phases, *Trends Chem.* **1**, 210 (2019).
- [4] M. Naguib, M. Kurtoglu, V. Presser, J. Lu, J. Niu, M. Heon, L. Hultman, Y. Gogotsi and M. W. Barsoum, Two-dimensional

nanocrystals produced by exfoliation of Ti_3AlC_2 , *Adv. Mater.* **23**, 4248 (2011).

- [5] B. Anasori, M. R. Lukatskaya, and Y. Gogotsi, 2D metal carbides and nitrides (MXenes) for energy storage, *Nat. Rev. Mater.* **2**, 16098 (2017).
- [6] T. Lapauw, K. Lambrinou, T. Cabioch, J. Halim, J. Lu, A. Pesach, O. Rivin, O. Ozeri, E. N. Caspi, L. Hultman, P. Eklund, J. Rosén, M. W. Barsoum, and J. Vleugels, Synthesis of the new MAX phase Zr_2AlC , *J. Eur. Ceram. Soc.* **36**, 1847 (2016).

- [7] B. Tunca, T. Lapauw, R. Delville, D.R. Neuville, L. Hennet, D. Thiaudière, T. Ouisse, J. Hadermann, J. Vleugels and K. Lambrinou, Synthesis and characterization of double solid solution $(\text{Zr, Ti})_2(\text{Al, Sn})$ C MAX phase ceramics, *Inorganic Chem.* **58**, 6669 (2019).
- [8] T. Lapauw, B. Tunca, T. Cabioc'h, J. Vleugels and K. Lambrinou, Reactive spark plasma sintering of Ti_3SnC_2 , Zr_3SnC_2 and Hf_3SnC_2 using Fe, Co or Ni additives, *J. Euro. Ceram. Soc.* **37**, 4539 (2017).
- [9] T. Ito, D. Pinek, T. Fujita, M. Nakatake, S.I. Ideta, K. Tanaka and T. Ouisse, Electronic structure of Cr_2AlC as observed by angle-resolved photoemission spectroscopy, *Phys. Rev. B* **96**, 195168 (2017).
- [10] D. Pinek, T. Ito, M. Ikemoto, M. Nakatake and T. Ouisse, Electronic structure of V_2AlC , *Phys. Rev. B* **98**, 035120 (2018).
- [11] D. Pinek, T. Ito, M. Ikemoto, K. Yaji, M. Nakatake, S. Shin and T. Ouisse, Unified description of the electronic structure of M_2AC nanolamellar carbides, *Phys. Rev. B* **100**, 075144 (2019).
- [12] D. Pinek, T. Ito, K. Furuta, Y. Kim, M. Ikemoto, S.I. Ideta, K. Tanaka, M. Nakatake, P. Le Fèvre, F. Bertran and T. Ouisse, Near Fermi level Ti_3SiC_2 electronic structure revealed by angle-resolved photoemission spectroscopy, *Phys. Rev. B* **102**, 075111 (2020).
- [13] M. Barbier, F. Wilhelm, D. Pinek, K. Furuta, T. Ito, Y. Kim, M. Magnier, D. Braithwaite, M. Vališka, C. Opagiste, M.W. Barsoum, P. Ohresser, E. Otero, P. Le Fèvre, F. Bertran, G. Gabarino, A. Rogalev and T. Ouisse, $\text{Mo}_4\text{Ce}_4\text{Al}_7\text{C}_3$: A nanolamellar Ferro-magnetic Kondo Lattice, *Phys. Rev. B* **102**, 155121 (2020).
- [14] D. Pinek, T. Ito, K. Furuta, A.J. van Bunningen, P. Le Fèvre, F. Bertran and T. Ouisse, Fermi surface and band structure of Ti_2SnC as observed by angle-resolved photoemission spectroscopy, *Phys. Rev. B* **104**, 195118 (2021).
- [15] S. Tanuma, C. J. Powell, and D. R. Penn, Calculations of electron inelastic mean free paths. IX. Data for 41 elemental solids over the 50 eV to 30 keV range, *Surf. Interface Anal.* **43**, 689 (2011).
- [16] J. Ren, L. Fu, G. Bian, M. Wong, T. Wang, G. Zha, W. Jie, T. Miller, M. Z. Hasan and T.-C. Chiang, Spectroscopic studies of $\text{CdTe}(111)$ bulk and surface electronic structure, *Phys. Rev. B* **91**, 235303 (2015).
- [17] J. Krempasky, V.N. Strocova, P. Blaha, L. Pattheya, M. Radovic, M. Faluba, M. Shi and K. Hricovini, Bulk vs. surface effects in ARPES experiment from $\text{La}_{2/3}\text{Sr}_{1/3}\text{MnO}_3$ thin films, *J. Electron. Spectrosc. Relat. Phenom.* **181**, 63 (2010).
- [18] M. Dendzik, M. Bianchi, M. Michiardi, C. E. Sanders and P. Hofmann, Reconstruction-induced trefoil knot Fermi contour of $\text{Au}(111)$, *Phys. Rev. B* **94**, 201401(R) (2016).
- [19] N. Olszowska and J. J. Kolodziej, Electronic structure of reconstructed $\text{InAs}(001)$ surfaces — identification of bulk and surface bands based on their symmetries, *Surf. Sci.* **644**, 95 (2016).
- [20] B. Yan and C. Felser, Topological materials: Weyl semimetals, *Annu. Rev. Condens. Matter Phys.* **8**, 337 (2017).
- [21] S. R. Park, J. Han, C. Kim, Y. Y. Koh, C. Kim, H. Lee, H. J. Choi, J. H. Han, K. D. Lee, N. J. Hur, M. Arita, K. Shimada, H. Namatame and M. Taniguchi, Chiral orbital-angular momentum in the surface states of Bi_2Se_3 , *Phys. Rev. Lett.* **108**, 046805 (2012).
- [22] J.-H. Park, C. H. Kim, J.-W. Rhim, and J. H. Han, Orbital Rashba effect and its detection by circular dichroism angle-resolved photoemission spectroscopy, *Phys. Rev. B* **85**, 195401 (2012).
- [23] T. Hoshi, Y. Iguchi and T. Fujiwara, Nanoscale structures formed in silicon cleavage studied with large-scale electronic structure calculations: Surface reconstruction, steps, and bending, *Phys. Rev. B* **72**, 075323 (2005).
- [24] A. Gkoutaras, Y. Kim, J. Coraux, V. Bouchiat, S. Lisi, M. W. Barsoum and T. Ouisse, Mechanical exfoliation of select max phases and $\text{Mo}_4\text{Ce}_4\text{Al}_7\text{C}_3$ single crystals to produce maxenes, *Small* **16**, 1905784 (2020).
- [25] T. Ouisse, E. Sarigiannidou, O. Chaix-Pluchery, H. Roussel, B. Doisneau and D. Chaussende, High temperature solution growth and characterization of Cr_2AlC MAX phase single crystals, *J. Cryst. Growth* **384**, 88 (2013).
- [26] L. Shi, T. Ouisse, E. Sarigiannidou, O. Chaix-Pluchery, H. Roussel, D. Chaussende and B. Hackens, Synthesis of single crystals of V_2AlC phase by high temperature solution growth and slow cooling technique, *Acta Mater.* **83**, 304 (2015).
- [27] F. Mercier, T. Ouisse and D. Chaussende, Morphological instabilities induced by foreign particles and Ehrlich-Schwoebel effect during the two-dimensional growth of crystalline Ti_3SiC_2 , *Phys. Rev. B* **83**, 075411 (2011).
- [28] J. P. Perdew, K. Burke, and M. Ernzerhof, Generalized gradient approximation made simple, *Phys. Rev. Lett.* **77**, 3865 (1996).
- [29] A. Kokalj, Computer graphics and graphical user interfaces as tools in simulations of matter at the atomic scale, *Comput. Mater. Sci.* **28**, 155 (2003).